Open Ceramics 17 (2024) 100533

Contents lists available at ScienceDirect

Open Ceramics

journal homepage: www.sciencedirect.com/journal/open-ceramics

Fracture resistance of binderless tungsten carbide consolidated by spark plasma sintering and flash sintering

Isacco Mazo [a,b,*], Miguel A. Monclus [d], Jon M. Molina-Aldareguia [c,d], Vincenzo M. Sglavo [a,e]

[a] Department of Industrial Engineering, University of Trento, via Sommarive 9, Trento, Italy
[b] Institut Clément Ader (ICA), Université de Toulouse, CNRS, IMT Mines Albi, INSA, ISAE-SUPAERO, UPS, Campus Jarlard, F-81013, Albi, France
[c] Mechanical Engineering, Universidad Politécnica de Madrid, 28006, Madrid, Spain
[d] IMDEA Materials Institute, C/ Eric Kandel 2, 28906, Getafe, Madrid, Spain
[e] INSTM, National Interuniversity Consortium of Materials Science and Technology, Trento Research Unit, Via G. Giusti 9, 50123, Firenze, Italy

ARTICLE INFO

Handling Editor: Dr P Colombo

Keywords:
Binderless tungsten carbide
Electric current-assisted sintering (ECAS)
Spark plasma sintering (SPS)
Flash sintering (FS)
Indentation fracture resistance

ABSTRACT

Binderless tungsten carbide (WC) consolidated by spark plasma sintering (SPS) and electrical resistance flash sintering (ERFS) has emerged as a promising alternative to materials obtained by traditional sintering methods. In this study, we investigated the influence of SPS and ERFS techniques on the mechanical properties of binderless WC. Hardness, indentation fracture resistance and elastic modulus were compared and analysed with respect to the microstructure of the resulting material. The results show that SPS tungsten carbide is harder, stiffer and denser when compared to the material produced by ERFS. Nevertheless, the fracture resistance of SPS ceramics was limited due to the lack of macroscopic toughening mechanisms. Conversely, flash-sintered tungsten carbide, consolidated by ERFS, possesses unique biphasic WC/W_2C microstructures that promote crack deflection and bridging toughening mechanisms. Additionally, flash-sintered materials exhibit a more ductile character and are characterised by a lower effect of the strain gradient on the material plasticity upon indentation. This study provides valuable insights into the mechanical properties of ultra-hard monolithic ceramics, such as WC, influenced by ultrafast/flash sintering techniques.

1. Introduction

Tungsten carbide (WC) is a well-known and widely used refractory ceramic material due to its excellent mechanical properties, including high hardness, wear resistance, and toughness [1]. However, the traditional sintering process used for its consolidation involves the addition of a binder, which can compromise its high-temperature mechanical properties, particularly its hardness and wear resistance [2,3]. Binderless tungsten carbide (BTC) consolidated by spark plasma sintering (SPS) and electrical resistance flash sintering (ERFS) has recently emerged as promising alternatives to traditional sintering methods [4–6]. In recent years, there has been a growing interest in the development of tungsten carbide components for applications at high temperature and/or in harsh environments [5] and the mechanical properties of the consolidated materials are critical for their performance and durability. Therefore, it is essential to understand how the consolidation technique can influence the mechanical properties of binderless WC.

SPS and ERFS are, respectively, fast and ultrafast consolidation techniques that can produce dense, fine-grained pure WC. SPS couples high uniaxial pressure (50–60 MPa) with fast heating (50–500 °C/min) by applying a pulsed electric current to a conductive graphite die surrounding the powder compact [7,8] Conversely, in ERFS, a thermal runaway event is activated within the powder compact by an alternated electric field, resulting in a much more rapid temperature increase (10^3-10^4 °C/min) and quick densification [6]. While both techniques have been demonstrated to produce high-density tungsten carbide, the effects of their different sintering kinetics on the mechanical properties of the resulting materials have not been clarified yet.

The aim of this study is to investigate the influence of SPS and ERFS on the mechanical properties of binderless WC. Specifically, hardness, indentation fracture resistance and elastic modulus of WC consolidated by these two techniques are compared and correlated with the generated microstructure. This work contributes to a better understanding of the

* Corresponding author. Department of Industrial Engineering, University of Trento, via Sommarive 9, Trento, Italy.
E-mail addresses: isacco.mazo@mines-albi.fr (I. Mazo), miguel.monclus@imdea.org (M.A. Monclus), jon.molina@imdea.org (J.M. Molina-Aldareguia), vincenzo.sglavo@unitn.it (V.M. Sglavo).

https://doi.org/10.1016/j.oceram.2023.100533
Received 25 September 2023; Received in revised form 19 December 2023; Accepted 23 December 2023
Available online 23 December 2023

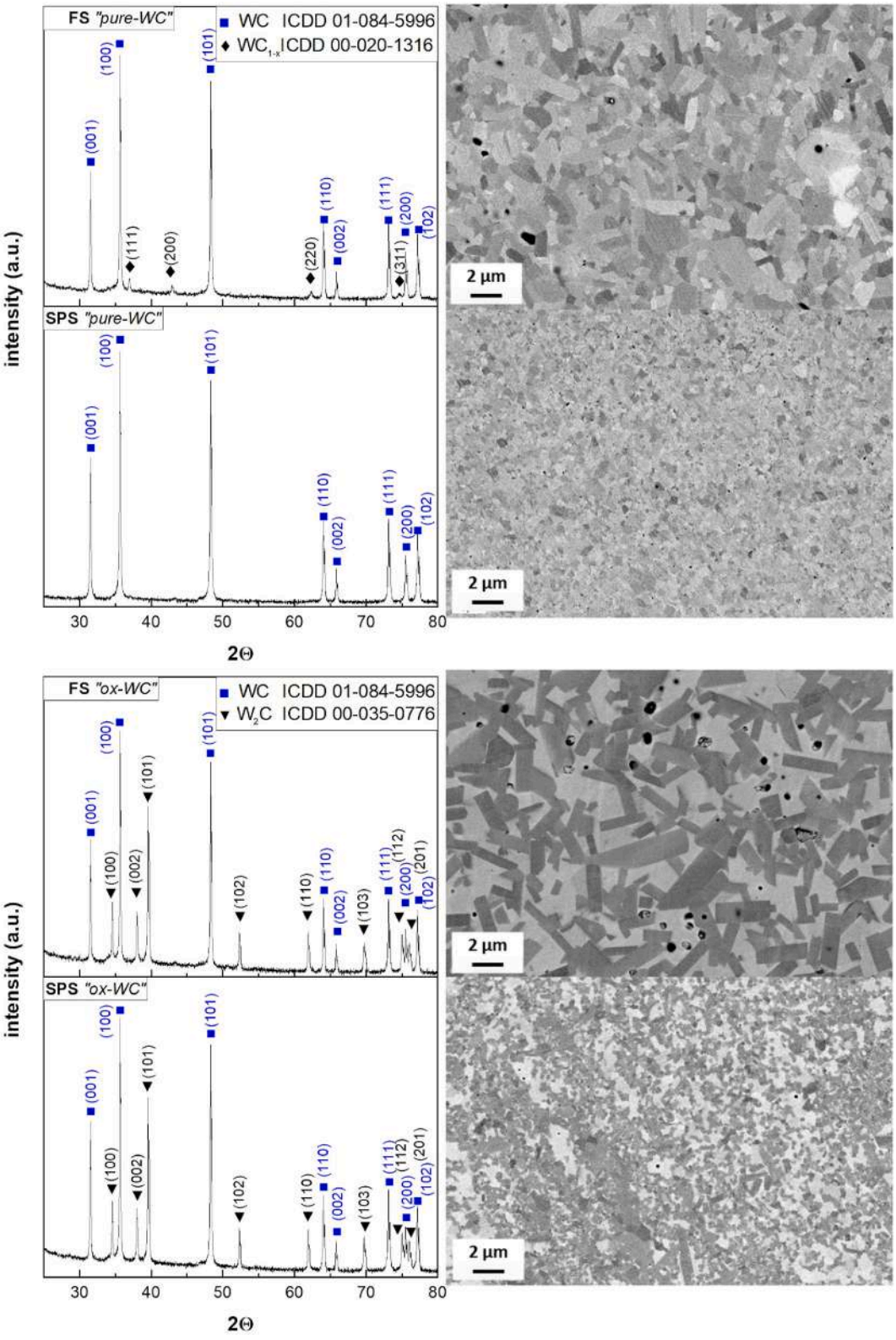

Fig. 1. Phase composition (XRD) and microstructure (FESEM-BSE) of the FS_{ox}, FS_{pure}, SPS_{ox} and SPS_{pure} samples.

consolidation techniques' influence on the mechanical properties of binderless WC and to provide insights into the development of high-performance WC-based materials useful for harsh environment applications.

2. Experimental procedures

2.1. Sample preparation

Four monolithic WC samples with different phase compositions were produced by ultrafast ERFS and fast SPS techniques (Fig. 1). During

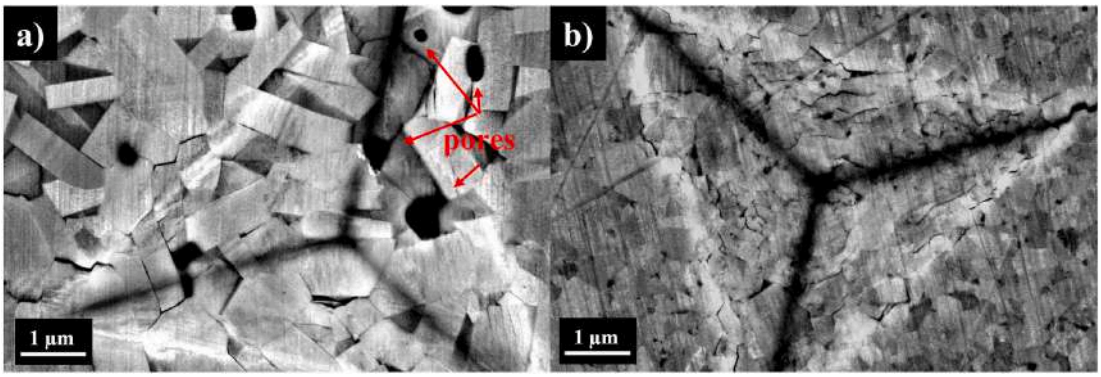

Fig. 2. Example of Berkovich imprints on FS_{pure} (a) and SPS_{pure} (b) samples at 750 mN.

ERFS practice, a green cylindrical pellet of WC powder is flash-sintered within an electrically insulating hBN/ZrO_2 ceramic die. The conditions for flash sintering in WC powders are achieved at room temperature and low pressure (4 MPa) upon the application of a moderate alternated electric field (5–6 V/cm) through a high current step-down transformer (TECNA® item 3870) [6]. The powdered material densifies very rapidly during the flash event, reaching up to 95 % relative density in the first 10 s thanks to a sintering rate as high as 0.2–0.3 s^{-1}. The specimens used for the present work were consolidated under 4 MPa uniaxial pressure, 3.7 V and 1000 A, for a total duration of 10 s. On the other hand, in the SPS practice, full consolidation occurs in a time scale of about 15 min under 50 MPa uniaxial pressure during a fast-sintering cycle (heating rate = 200 °C/min up to the maximum temperature, 2100 °C, followed by 5 min holding time). The sintering rate during SPS is the range of 0.005–0.01 s^{-1}, which is more than one order of magnitude lower than ERFS. This tenfold difference in the time scale for densification is indeed referred to as fast (SPS) and ultrafast (ERFS) sintering in the following.

Two types of tungsten carbide (WC) nanopowders from Inframat Advanced Materials® were selected. The powders exhibit different oxygen content, equal to 1.21 wt% and 0.28 wt% for the oxidized (WC_{ox}) and purest one (WC_{pure}), respectively, as previously reported in Refs. [9,10]. Sintering of the oxidized nanopowders produced biphasic composites (WC/W_2C = 60/40 vol%) while single-phase material and metastable cubic WC_{1-x} phase embedded in the WC matrix were obtained by SPS and ERFS, respectively, for the pure powders. The specimens prepared in this study were labelled as FS_{ox}, SPS_{ox}, FS_{pure}, and SPS_{pure} according to their microstructure already reported in Ref. [11] and summarized in Fig. 1. The details of the two processes, as well as the composition and microstructure of the obtained materials, have been carefully described in previous works [6,11].

2.2. Nanoindentation

Elastic modulus and hardness were measured by an instrumented nanoindenter (Hysitron triboindenter TI950) equipped with a diamond Berkovich tip [12]. The hardness, H, was evaluated from the maximum load P_{max} and the contact area A_c:

$$H = \frac{P_{max}}{A_c} \tag{1}$$

The reduced modulus E_r was obtained from the unloading stiffness, S, following Oliver and Pharr method [13]; the specimen modulus, E_s,

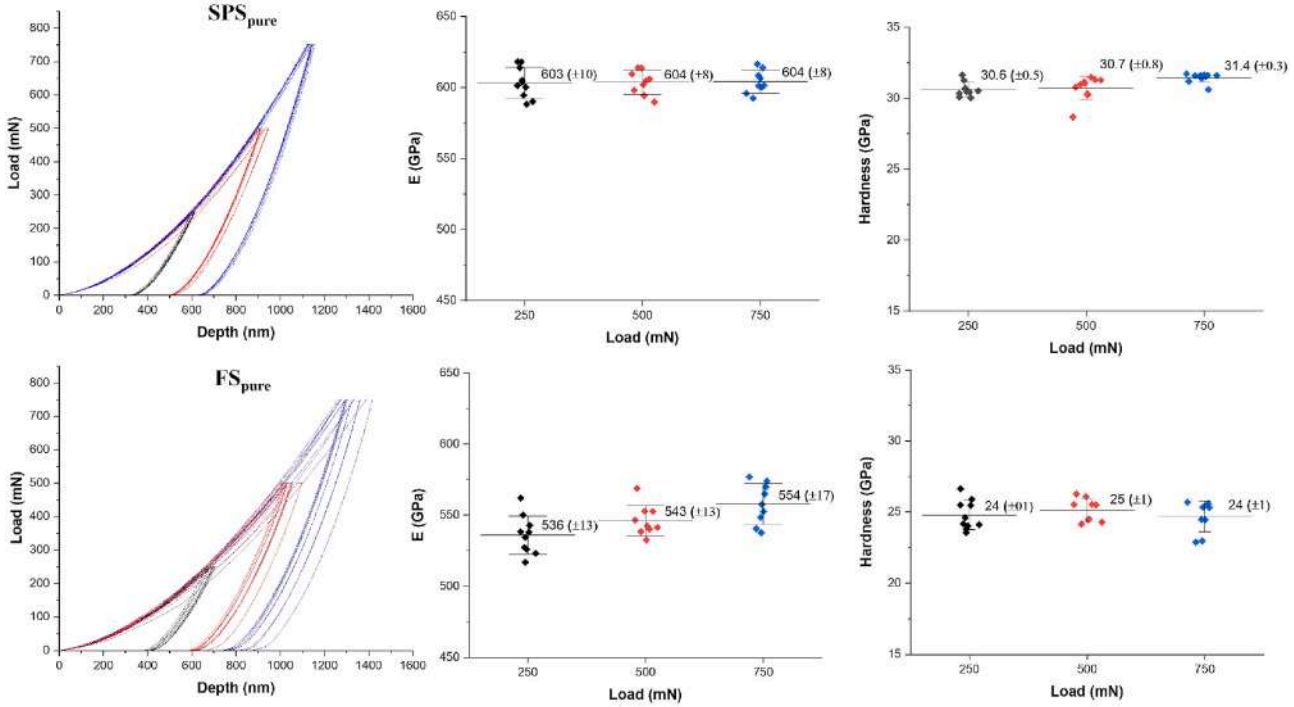

Fig. 3. Nanoindentation curves, modulus (specimen modulus E_s) and hardness for SPS_{pure} and FS_{pure} samples for maximum indentation load of 250, 500 and 750 mN.

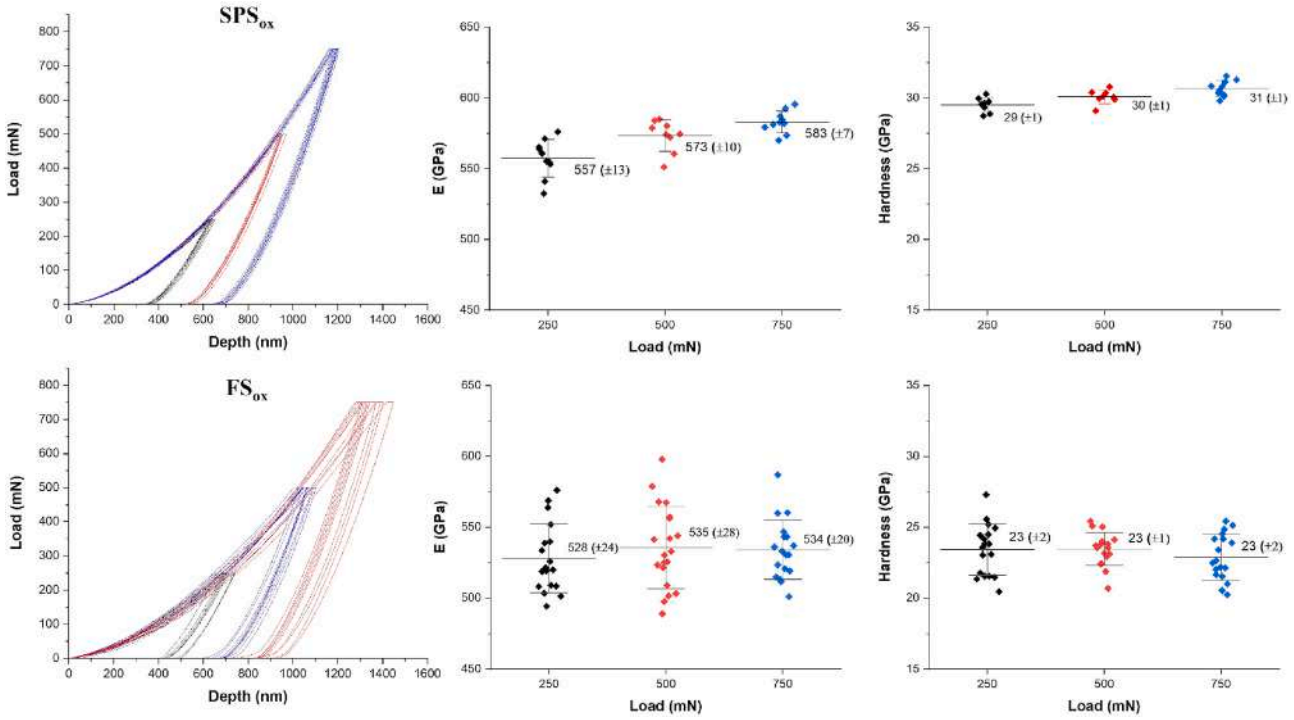

Fig. 4. Nanoindentation curves, modulus (specimen modulus Es) and hardness for SPS_{ox} and FS_{ox} samples for maximum indentation loads of 250, 500 and 750 mN.

was then calculated as:

$$\frac{1}{E_r} = \frac{(1-\nu_i^2)}{E_i} + \frac{(1-\nu_s^2)}{E_s} \quad (2)$$

where the modulus of the diamond indenter, E_i, = 1140 GPa, and its Poisson's ratio, ν_i, is 0.07,the Poisson's ratio, ν_s, of the specimen being assumed to be 0.19. Three maximum loads of 250, 500 and 750 mN were considered, with ten repetitions for each load.

Elastic modulus and hardness maps were generated on a specific area of interest, performing 22 x 22 indents in an area of 7.7 × 7.7 μm^2, using a 3 mN maximum load a separation distance of 350 nm between indents. The indentation map position was selected using the scanning probe microscopy (PSM) mode of the nanoindenter. In SPM mode, the nanoindenter tip scans the surface using a very low contact force (2 μN), giving a topography image of the surface.

2.3. Vickers indentation

Vickers hardness was measured at five different loads (100, 20, 20, 5 and 2 N) with 10 s holding time and ten replicas at each load. The indentation fracture resistance was measured by analysing the radial cracks generated on the surface of the samples upon indenter unloading.

The imprints were observed after the tests with a digital optical microscope (Olympus DSX1000) for a precise measurement of the radial cracks and further examined in the FEG-SEM microscope using a backscattered electrons (BSE) detector (ThermoFischer® Apreo 2S LoVac).

3. Results & discussion

3.1. Elastic modulus & hardness

A very high hardness, in excess of 23 GPa, characterizes the BTC samples as shown in Figs. 3 and 4, pointing out the high degree of densification and structural integrity of the materials sintered by both techniques. Nevertheless, the samples sintered by SPS are superior in both hardness and modulus at the three tested loads. SPS samples possess a hardness in the range 29–31 GPa, about 7 GPa more than the two FS samples. This difference can be mainly attributed to the finer microstructure and smaller grains size produced by SPS (Fig. 1). Conversely, the large difference in the elastic modulus is more difficult to explain by considering only the microstructure. The SPS_{pure} sample possesses a modulus of about 600 GPa, around 70 GPa higher than FS_{pure} one, a difference that can not be ascribed to the grain size. In addition, samples with a large second phase (W_2C) content, namely FS_{ox} and SPS_{ox} (Fig. 4), are instead characterized by a similar average modulus of 530–550 GPa; this value is in between the modulus of its two components, 700 GPa for WC [14–16] and 440 GPa for W_2C (Fig. 5) [17,18]. The larger scatter observed in Fig. 4 for the elastic modulus of FS_{ox} can surely be ascribed to the very coarse microstructure; in other words, the result from the indentation analysis depends on the specific phase sampled by the diamond tip (Fig. 5).

It is interesting to observe that the modulus for the FS_{pure} sample is not larger than in FS_{ox} despite the latter containing 40 vol% W_2C (Fig. 1), this phase being characterized by considerably lower E (Fig. 5).

Two are the possible causes for the different elastic response between FS_{pure} and SPS_{pure} materials (Fig. 3): (i) the residual porosity of about 3–4 vol%, it being known to affect the modulus if the indenter size is comparable with the size of the pores, like in the imprint of Fig. 2 (a) [19,20]; (ii) the presence of 8–10 vol% of WC_{1-x} second phase, characterised by a much lower modulus ≅ 300 GPa [10].

The hardness was also measured from Vickers indentation at different loads (Fig. 8). It is clear that this correspond to a macroscopic value where the presence of different phases and grain size in the material are averaged. In general, hardness decreases with the applied maximum load. At the lowest load (2 N), the SPS samples reach a Vickers hardness that is comparable with that obtained by nanoindentation (Figs. 3 and 4), around 30 GPa for the biphasic SPS_{ox} and above 31 GPa for monophasic SPS_{pure}. Similarly, for the flash sintered samples, the hardness drops to 24–25 GPa for the FS_{pure} and about 21 GPa for biphasic FS_{ox}.

This behaviour, known as indentation size effect (ISE), has several possible contributions that depends on the material's plasticity. In very hard ceramics, the deformation under the indenter occurs in discrete

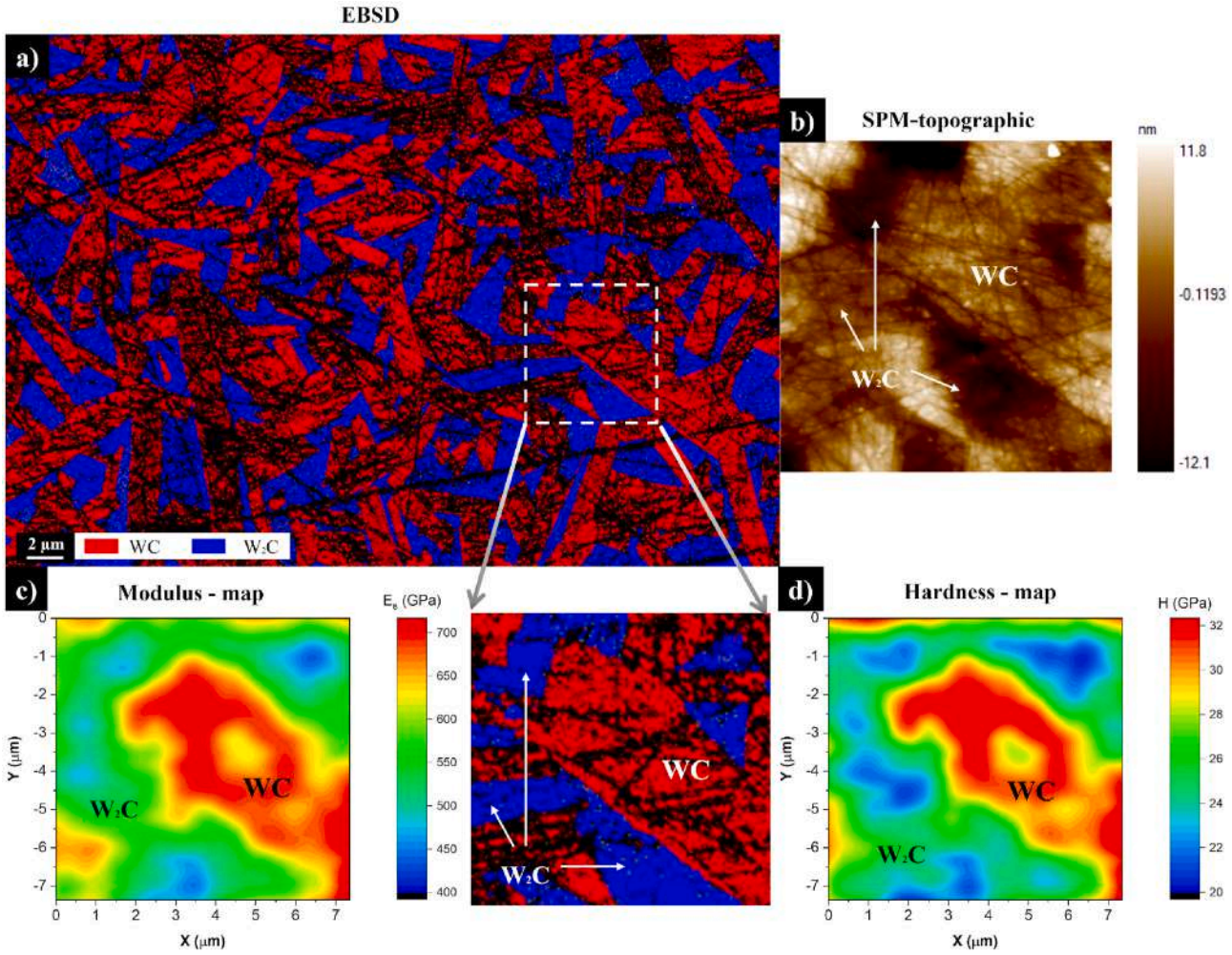

Fig. 5. EBSD phase composition of FS_{ox} (a) is reported together with the SPM imaging (b) and properties mapping (c, d) of the area selected by the dotted white rectangle.

bands rather being continuous. The recovery of the elastic increment of deformation, preceding each new band of deformation, results in the indentation appearing smaller than expected. Since this effects scale with the indentation size, lower is the applied loads and higher is the magnitude of the elastic recovery between two deformation bands [21]. Bull et al. reported that in some extreme cases, when the indentation is in the nano size, the surface flexure will remain elastic and is fully recovered upon unloading, leaving no residual hardness impressions [21].

3.2. Indentation fracture resistance

The determination of fracture resistance by indentation method requires the correct determination of the crack shape, which, theoretically can be Palmqvist or median-radial (Fig. 6). The type of crack depends on the material and the indentation load [22]. Since both crack systems appear substantially the same on the surface, the only way to determine the real system is a direct examination of the fracture surface [23]. The determination of the system is very important for this kind of analysis since it regulates the correct equation to be used for the determination of the indentation fracture resistance [24]. WC-based materials can show different types of cracks depending on the presence of the metallic binder. WC-Co cermets show Palmqvist crack type and their indentation toughness is generally measured using the Shetty equation [25]. For binderless materials the situation is more complex and the choice of the equation is not unique among the scientific community; some researcher used the Anstis equation [26] (median-radial crack type) [27], while others used the Shetty one (Palmqvist crack type) [28,29]. This result in a certain confusion in the reported fracture resistance values [14], since the two equations can lead to difference in the estimated fracture resistance of about 2–3 MPa $m^{1/2}$, which, in a brittle material like pure WC, is equivalent to an error larger than 40 %.

In the present study, the crack geometry was directly determined by observing the surface (Fig. 7) generated by a manual fracture of the specimens containing a Vickers indentation performed at 98 N. Fig. 7(b) clearly shows that, at this specific applied load, the generated crack is median-radial (Fig. 6, b). This same crack morphology was assumed to characterize the indentations performed at lower loads.

Therefore, the Anstis formalism can be used to determine the indentation fracture resistance:

$$K_{Ic} = 0.016\left(\frac{E}{H}\right)^{\frac{1}{2}}\left(\frac{P}{c^{\frac{3}{2}}}\right) \quad (3)$$

P being the indentation load, c the average crack length (Fig. 6), H the hardness and E the Young's modulus previously measured from the nanoindentation tests.

The fracture resistance of SPS samples is around 4–5 MPa $m^{0.5}$, in agreement with the data reported in the literature [30]. Slightly lower values are measured on SPS_{ox} material which contains larger amount of W_2C phase, which is generally considered more brittle ($K_{Ic} \cong$ 3.5 MPa $m^{0.5}$ [31]). In the biphasic and monophasic SPS samples K_{Ic} is substantially constant with the indentation load. On the other hand, the FS

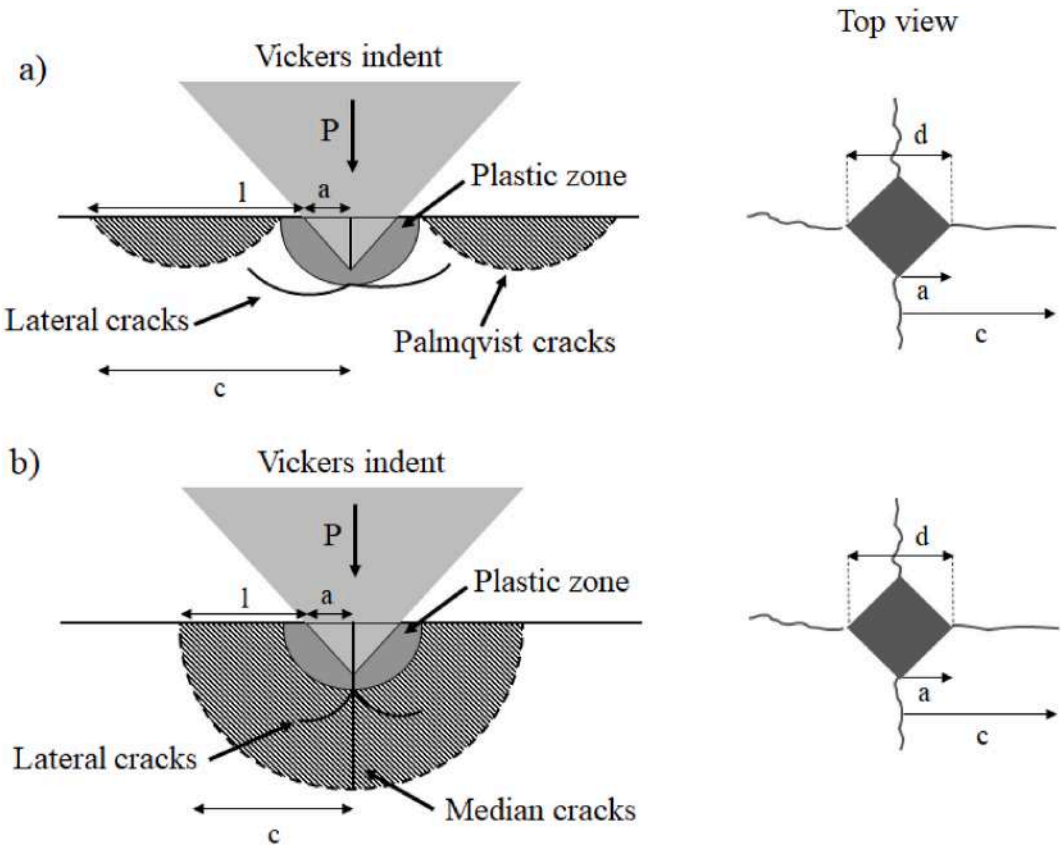

Fig. 6. Crack profile in Palmqvist (a) and median-radial (half-penny) cracks (b).

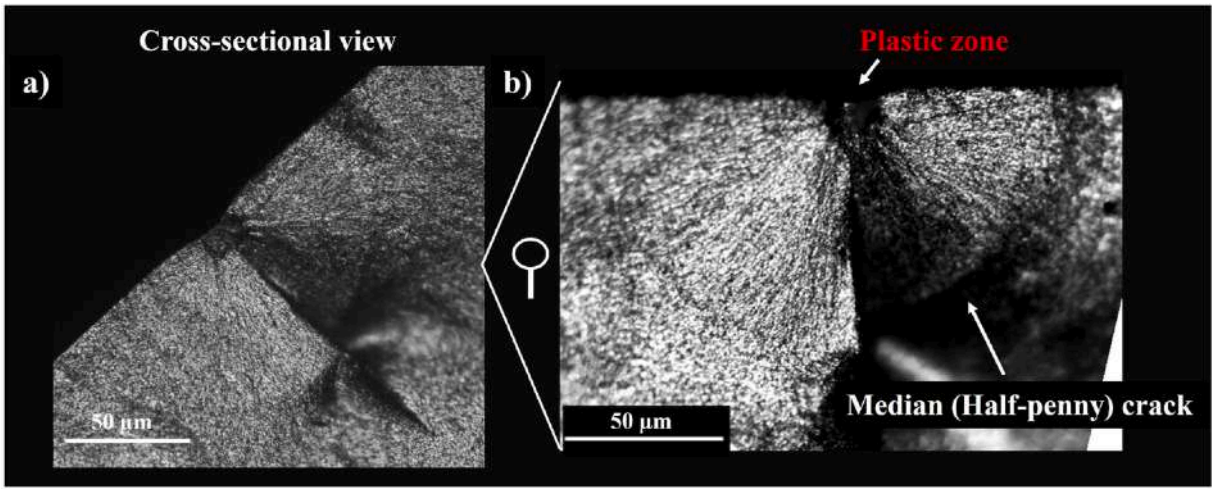

Fig. 7. Crack cross-section profile of a Vickers indent performed at 10 kg on the surface of a BTC component (a) and its magnified view showing a median-radial (half-penny) crack morphology (b).

specimens show an overall higher K_{Ic} which increases by decreasing the indentation load. Fracture resistance for FS_{pure} material but especially for biphasic FS_{ox} samples is considerably higher than in the SPS counterpart, reaching values of ≅ 6–7 MPa $m^{0.5}$ and 8–9 MPa $m^{0.5}$, respectively. This difference can be visualised in Fig. 12, where all the indentation crack lengths used to evaluate K_{Ic} (Eq. (3)) are reported.

The large difference in fracture resistance between FS_{ox} and SPS_{ox} is easily discernible from Fig. 9, where the indentation crack lengths generated by Vickers indentation loads of 20, 10 and 5 N are compared. Radial cracks in the flash sintered material are visibly shorter and, even more importantly, they appear highly tortuous. For loads lower than 5 N radial cracks are not even visible on the surface. Accordingly, the corresponding K_{Ic} value at low loads in Fig. 8 is only estimated from the size of the hardness imprint.

The relatively large toughness of the WC/W_2C biphasic material was also revealed from micropillar compression tests reported in a previous work [11], the biphasic micropillars retaining a large portion of their strength (≅ 6 GPa) up to considerably large deformations (8 % strain).

The capability of FS_{ox} material to dissipate large amount of strain energy for crack propagation is for sure connected with crack deflection

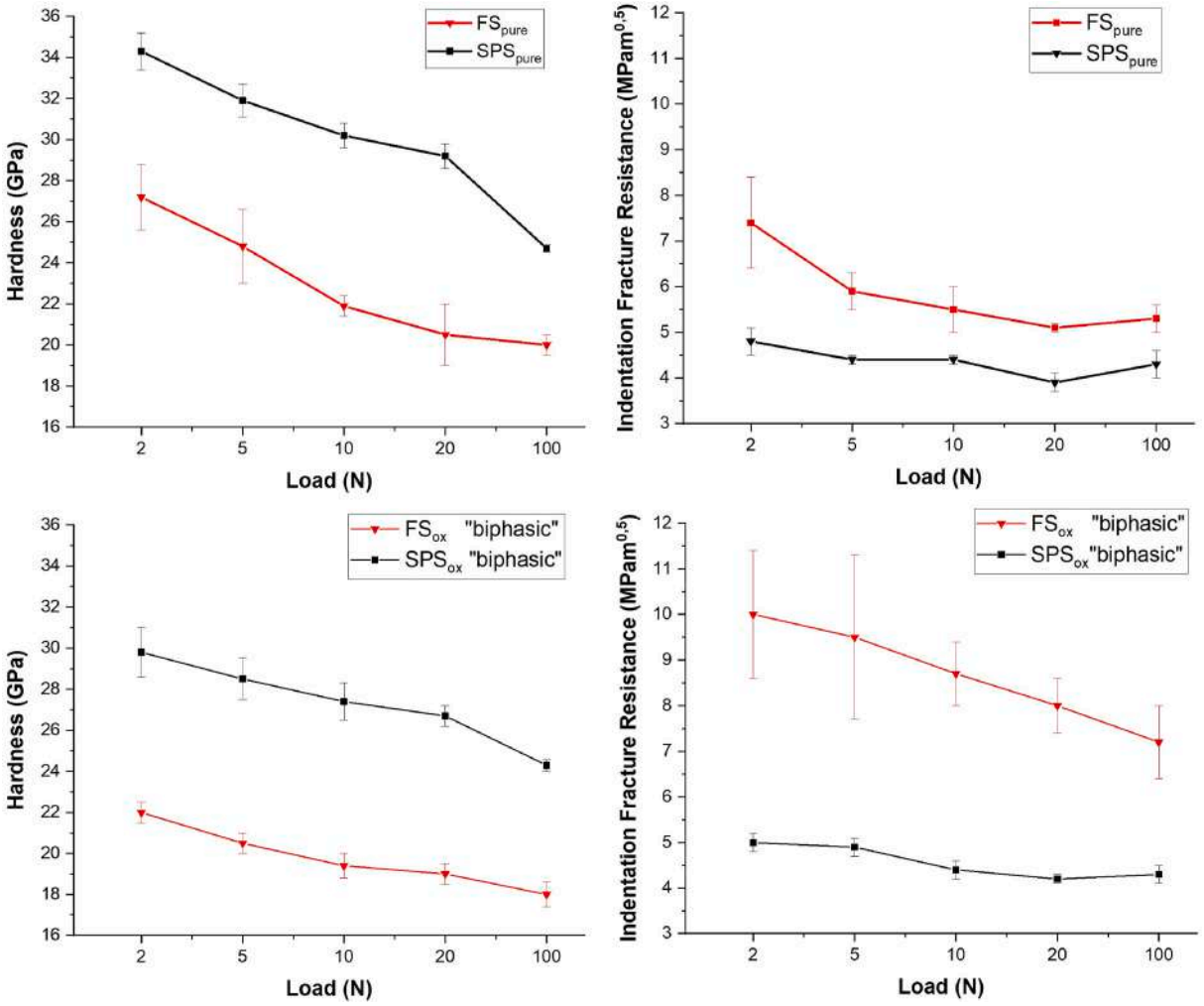

Fig. 8. Vickers hardness and indentation fracture resistance of the four BTC samples measured at different loads: 2, 5, 10, 20 and 100 N.

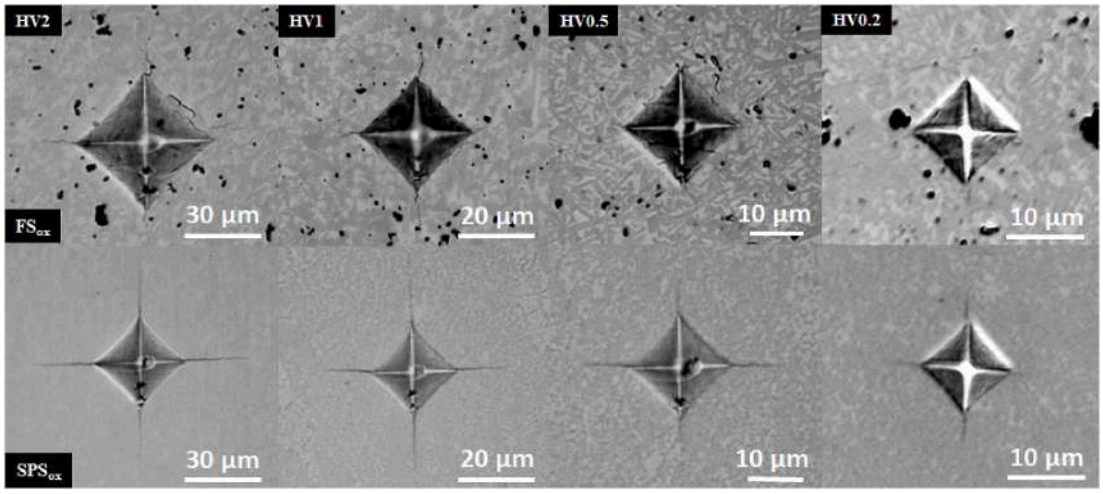

Fig. 9. Vickers indentations for FS$_{ox}$ (top) and SPS$_{ox}$ (bottom) at different maximum loads.

and bridging toughening mechanism as shown by the SEM micrographs in Fig. 10. The difference in the mechanical properties of WC and W_2C phases (Fig. 5) creates a condition similar to that schematized in Fig. 10 (e, f) where hard particles are dispersed in a softer matrix. Such toughening mechanisms can only explain a flat increase in the K_{Ic} measured between FS$_{ox}$ and SPS$_{ox}$, but not an increase of K_{Ic} at lower indentations loads (Fig. 8). Also for FS$_{pure}$ the higher indentation fracture resistance of Fig. 8 corresponds to observable difference in the average crack length developed upon indentation (Fig. 12) similarly for FS$_{ox}$, below a certain critical load ($\leq$5 N) no indentation cracks are

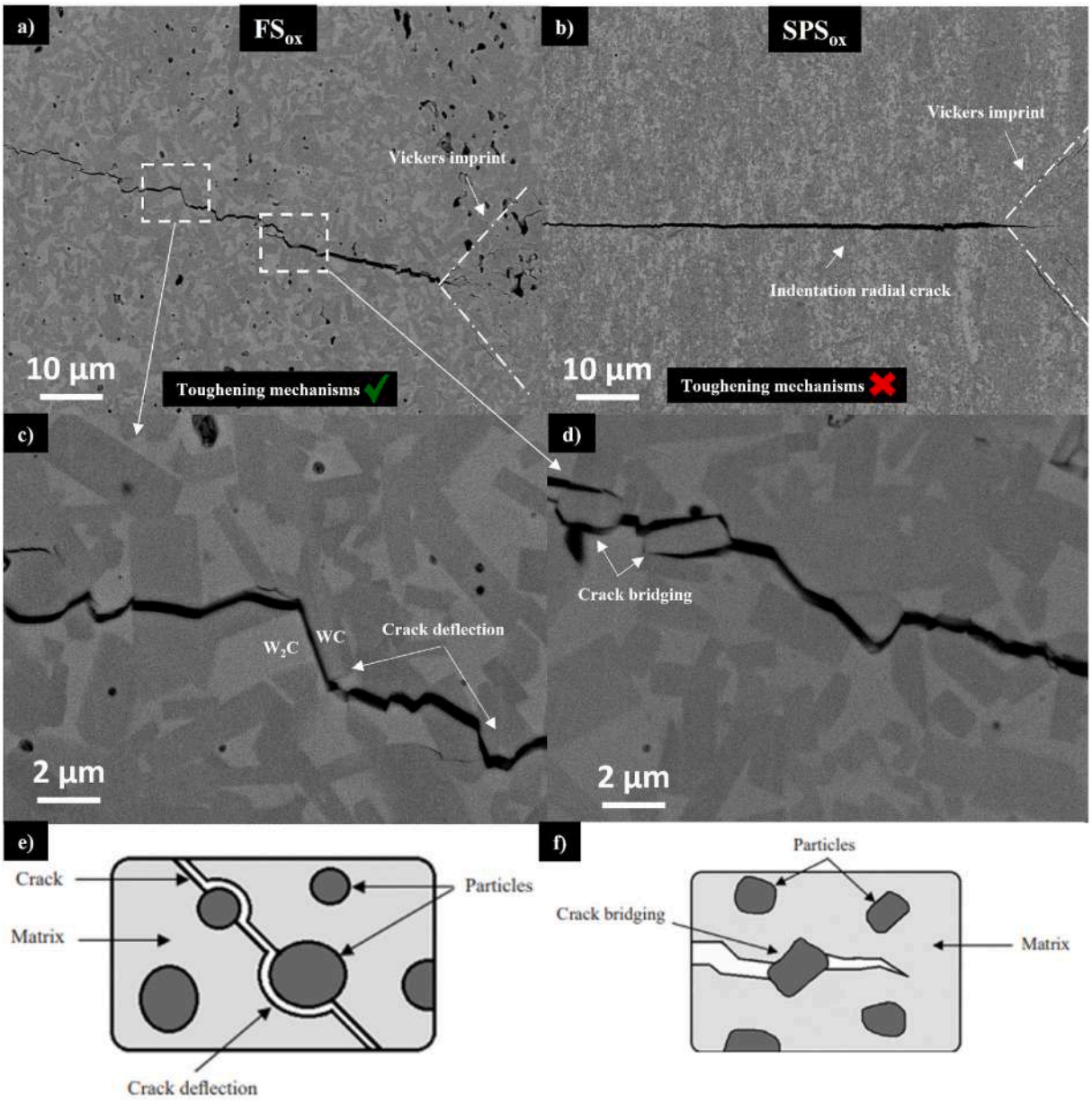

Fig. 10. Comparison of the radial crack morphology after 10 N Vickers indentation for FS_{ox} (a) and SPS_{ox} (b) samples. Crack deflection (c, e) and crack bridging (d, f) toughening mechanisms are active in the FS_{ox} material thanks to the presence of elongated WC grains in a WC/W_2C biphasic microstructure.

formed (Fig. 11). The investigation will now focus on the source of the indentation size effect (ISE) concerning fracture resistance in accounting for these issues, along with exploring any potential link to the enhanced toughness observed in the FS samples.

It is worth noting that the Anstis method (Eq. (3)) for the fracture resistance evaluation using Vickers indentation can be inaccurate for real cracks. Quinn and Bradt [32] highlighted various reasons for this. Real cracks possess bluntness and roughness, deviating from the assumption of a perfectly sharp crack. Incomplete closure of cracks during indentation leads to errors in measured crack length. Microstructural features like grain boundaries and residual stresses are not accounted for, affecting the indentation fracture resistance calculations. The method assumes plane strain conditions, but deformation may extend beyond the confined region, compromising accuracy. To summarise, the Anstis method overlooks real crack characteristics, incomplete closure, microstructural influences, and deviations from plane strain conditions, possibly leading to uncertainty in the toughness data presented in Fig. 8. Considering the large discrepancy presented by Quinn and Bradt on the K_{IC} measured by various indentation fracture resistance techniques with respect to the real K_{IC} of standardised test specimen, the results from indentation toughness are presented to compare the "*complex crack arrest phenomenon* [32]" of WC samples sintered by the two said techniques (SPS and FS).

In the forthcoming sections, the Indentation Size Effect (ISE) on hardness is analysed to investigate whether flash-sintered materials are inherently more prone to plastic deformation.

The ISE is influenced by the material's plasticity. For more ductile materials, ISE arises from the interplay of geometrically necessary dislocations (GND) and the statistically stored dislocations (SSD) [33,34], leading to higher hardness in smaller indentation due to larger strain gradient as depth increases. Conversely, for very hard materials, plastic deformation manifests in discrete bands, resulting in a more pronounced ISE at lower loads due to a greater elastic recovery [21,35].

The proportional specimen resistance (PSR) model delineates the elastic and plastic components influencing the ISE behaviour. This model offers a mathematical correlation between the indentation load

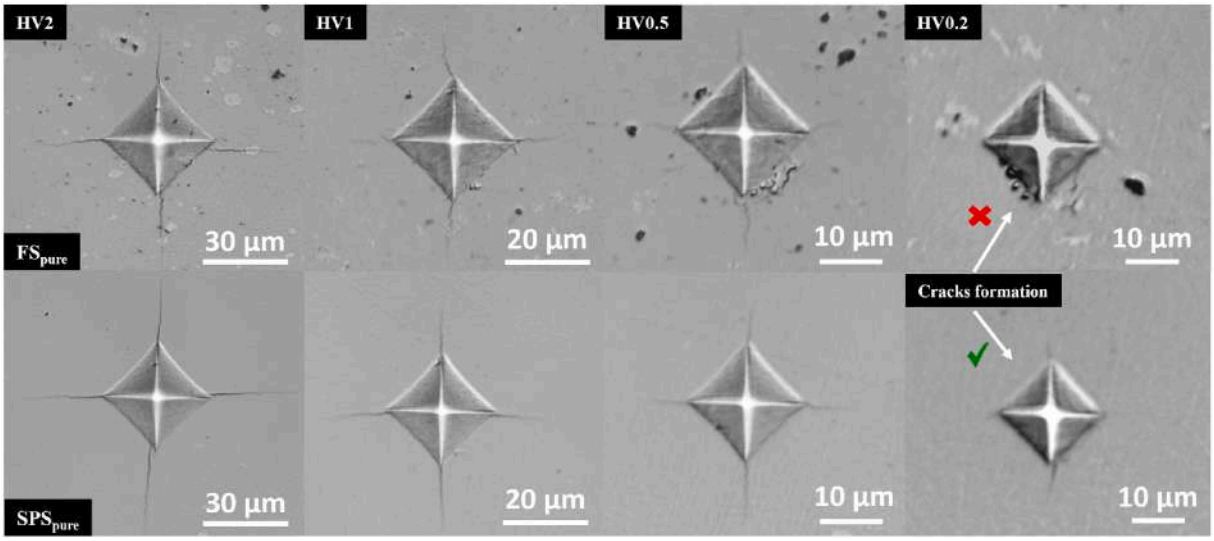

Fig. 11. Vickers indentation for FS_{pure} (top) and SPS_{pure} (bottom) at different maximum loads.

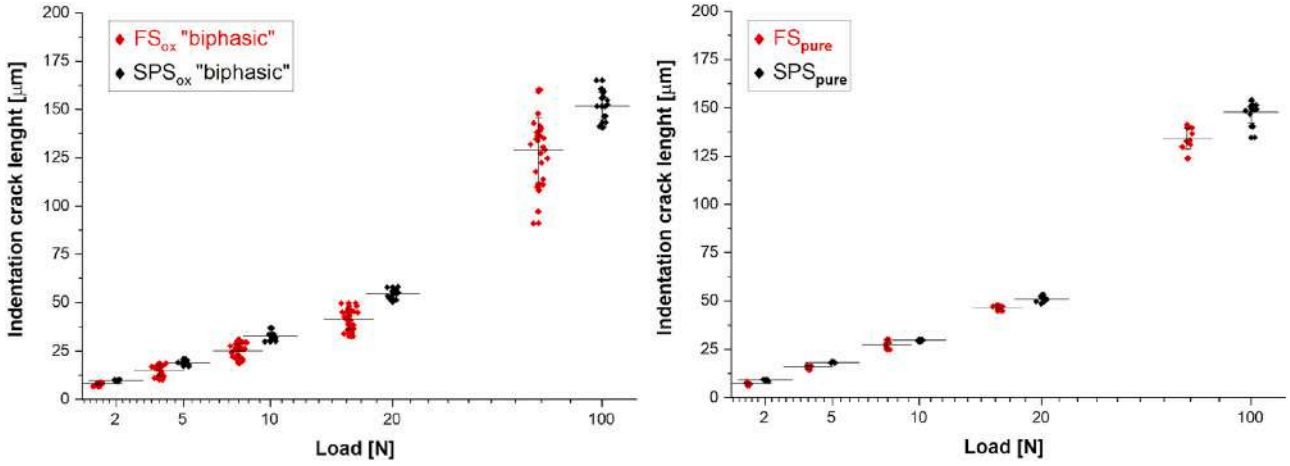

Fig. 12. Comparison of the indentation crack lengths in FS and SPS samples. The red dots are slightly shifted on the x-axis (log_{10}) for a representative purpose. (For interpretation of the references to colour in this figure legend, the reader is referred to the Web version of this article.)

and the diagonal indentation length, discriminating the analysis of deformation work in terms of surface work (elastic component) and volume work (plastic component) [35,36]. The indentation load, P, can be correlated with the diagonal length, d, as:

$$P = ad + bd^2 \tag{4}$$

where a and b are two constants of the system. If one considers the proportionality between the diagonal length (d) and the imprint depth (δ_{max}), the work for deformation can be represented by $W \cong \alpha_1 P d$ where $\alpha_1 = \frac{1}{2}\frac{\delta_{max}}{d}$.

Multiplying Eq. (4) by the diagonal length, d, one obtains:

$$P d = a d^2 + b d^3 \tag{5}$$

According to this representation, the first term ($a d^2$) is related to the indentation surface area while the second one is associated with the deformed volume. The first coefficient, a, is therefore proportional to the surface work, i.e., the combination of friction energy and elastic resistance energy (elastic contribution); b is proportional to the work performed to plastically deform the material under the indenter (plastic contribution) [37]. The two adimensional parameters, a and b, can be determined by plotting P/d versus d as in Fig. 13. While the elastic coefficients, a, is substantially similar among the tested samples of Fig. 8, one can notice a significative difference in b between the FS and the SPS samples. The significant drop of b implies that less work is necessary to permanently deform the FS materials under the indenter tip (Fig. 13).

The two FS samples showing increased toughness are also softer than the SPS ones. They are characterized by a lower elastic modulus, hardness, yield strength and plastic contribution to the ISE effect. Since this plastic contribution is connected to the strain gradient in the plastic zone, the decrease of b, as determined in Fig. 13, corresponds to a lower effect of the strain gradient over the indentation size effect (ISE).

A relatively high volume, equal to the submerged indenter volume, must be relocated somehow during indentation. This occurs easily for ductile material with a high dislocation activity like metals, but the situation is much more complex in ceramics, like WC. In this case, the material can be relocated by: (i) extensive microcracking, when they become interlinked, the material is allowed to dislodge, (ii) dislocation movement activated by high-stress levels and (iii) grain sliding in some particular cases. Usually, to accommodate plastic deformation below the indenter tip grains need to rotate according to the necessity of generating the geometrical necessary dislocations. The lower the load, the higher the strain gradient making the movement and the change in the direction of these dislocations much more difficult, experiencing a higher material's hardness. According to these concepts, the lower effect

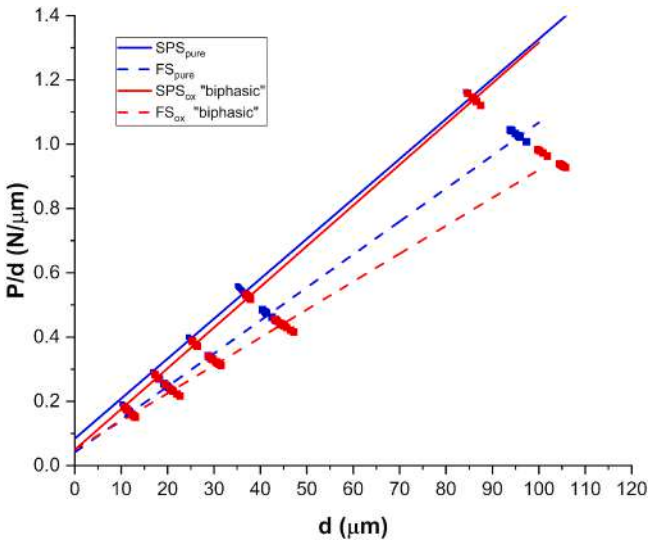

Fig. 13. Proportional specimen resistance (PSR) model: plot of P/d over d (diagonal length of indentation) for the evaluation of elastic (a) and the plastic (b) coefficients of Eq. (5).

of strain gradient on the ISE can be associated with (i) weaker GB, grains can be relocated at lower stresses by extensive microcracking without the necessity to activate deformation mechanisms or (ii) flash sintered WC grains are "softer" and more easily deformable than SPS ones.

It is difficult to discriminate which of the two effects is the most dominant during indentation. However, if both are present, they can give origin to an indentation size effect also for K_{Ic} as follows. When the indentation size is small, plastic mechanisms are favoured because the limited interaction volume limits the strain energy available for crack propagation. On the other hand, with the increase in the interaction volume, hence at higher indentation loads, the material is more prone to accommodate the permanent deformation by microcracking, hence is more fragile causing the drop in K_{IC} observed in Fig. 8 for the FS samples.

4. Conclusions

BTC ceramics produced by SPS are harder (30+ GPa), stiffer (≅600–700 GPa) and denser (98–99 %+) concerning the material consolidated by ERFS. From one side, SPS can densify pure WC powder with great control over the grain size and the phase composition, possibly retaining 100 % of α-WC in spite of W_2C or WC_{1-x} secondary phases. On the other side, SPS ceramics are intrinsically more brittle, with a fracture resistance K_{Ic} limited to 4–5 MPa $m^{0.5}$ because of the lack of any macroscopic toughening mechanisms. The ultra-fast sintering of pure WC leaves some residual porosity (3–4 vol%), which negatively affects the hardness (20–25 GPa) and modulus (≅550 GPa) of the bulk. However, it introduces some unique microstructural and mechanical features. It can produce biphasic WC/W_2C ceramics with toughness values almost twice higher (K_{Ic} ≅ 7–8 MPa $m^{0.5}$) than any SPS sample. Abnormal WC grains, 5–7 μm in size, with an elongated shape and surrounded by softer W_2C grains create the conditions for crack deflection and bridging toughening mechanisms. In addition, flash-sintered BTC ceramics present a "softer" character with respect to the SPS ones. They show an indentation size effect (ISE) on the fracture resistance; i.e. K_{Ic} increases by decreasing the indentation size. The separation of the elastic from the plastic contribution over the ISE behaviour points out that FS ceramics require less plastic work to plastically deform the material.

Funding

This work was partially supported within the program Departments of Excellence 2018–2022 (DII-UNITN "E-Mat") – funded by the Italian Ministry of University and Research (MIUR).

The authors are grateful to the JECS Trust for funding the visit of I. Mazo to IMDEA Materials Research Center, Madrid, Spain (Contract No. 2020255).

Declaration of competing interest

The authors declare that they have no known competing financial interests or personal relationships that could have appeared to influence the work reported in this paper.

References

[1] A.S. Kurlov, A.I. Gusev, Tungsten Carbides: Structure, Properties and Application in Hardmetals, Springer International Publishing, Cham, 2013, https://doi.org/10.1007/978-3-319-00524-9.
[2] G.S. Upadhyaya, Materials science of cemented carbides — an overview, Mater. Des. 22 (2001) 483–489, https://doi.org/10.1016/S0261-3069(01)00007-3.
[3] H.G. Schmidt, D. Marl, W. Benoit, C. Bonjour, The Mechanical Behaviour of Cemented Carbides at High Temperatures*, 1988.
[4] J. Zhang, G. Zhang, S. Zhao, X. Song, Binder-free WC bulk synthesized by spark plasma sintering, J. Alloys Compd. 479 (2009) 427–431, https://doi.org/10.1016/j.jallcom.2008.12.151.
[5] J. Sun, J. Zhao, Z. Huang, K. Yan, X. Shen, J. Xing, Y. Gao, Y. Jian, H. Yang, B. Li, A review on binderless tungsten carbide: development and application, Nano-Micro Lett. 12 (2020) 13, https://doi.org/10.1007/s40820-019-0346-1.
[6] I. Mazo, A. Molinari, V.M. Sglavo, Electrical resistance flash sintering of tungsten carbide, Mater. Des. 213 (2022) 110330, https://doi.org/10.1016/j.matdes.2021.110330.
[7] R. Chaim, Electric field effects during spark plasma sintering of ceramic nanoparticles, J. Mater. Sci. 48 (2013) 502–510, https://doi.org/10.1007/s10853-012-6764-9.
[8] R. Chaim, On densification mechanisms of ceramic particles during spark plasma sintering, Scripta Mater. 115 (2016) 84–86, https://doi.org/10.1016/j.scriptamat.2016.01.010.
[9] I. Mazo, L.E. Vanzetti, J.M. Molina-Aldareguia, A. Molinari, V.M. Sglavo, Role of surface carbon nanolayer on the activation of flash sintering in tungsten carbide, Int. J. Refract. Metals Hard Mater. (2022) 106090, https://doi.org/10.1016/j.ijrmhm.2022.106090.
[10] I. Mazo, J.M. Molina-Aldareguia, A. Molinari, V.M. Sglavo, Room temperature stability, structure and mechanical properties of cubic tungsten carbide in flash sintered products, J. Mater. Sci. (2023), https://doi.org/10.1007/s10853-022-08109-4.
[11] I. Mazo, M.A. Monclus, J.M. Molina-Aldareguia, V.M. Sglavo, M.M. Org, Does flash sintering alter the deformation mechanisms of tungsten carbide?, n.d. https://ssrn.com/abstract=4414639.
[12] I. Utke, J. Michler, R. Winkler, H. Plank, Mechanical properties of 3d nanostructures obtained by focused electron/ion beam-induced deposition: a review, Micromachines 11 (2020), https://doi.org/10.3390/MI11040397.
[13] W.C. Oliver, G.M. Pharr, Measurement of hardness and elastic modulus by instrumented indentation: advances in understanding and refinements to methodology, J. Mater. Res. 19 (2004) 3–20, https://doi.org/10.1557/jmr.2004.19.1.3.
[14] J. Sun, J. Zhao, Z. Huang, K. Yan, X. Shen, J. Xing, Y. Gao, Y. Jian, H. Yang, B. Li, A Review on Binderless Tungsten Carbide, Development and Application, 2020, https://doi.org/10.1007/s40820-019-0346-1.
[15] J.J. Roa, P. Sudharshan Phani, W.C. Oliver, L. Llanes, Mapping of mechanical properties at microstructural length scale in WC-Co cemented carbides: assessment of hardness and elastic modulus by means of high speed massive nanoindentation and statistical analysis, Int. J. Refract. Metals Hard Mater. 75 (2018) 211–217, https://doi.org/10.1016/j.ijrmhm.2018.04.019.
[16] S.J. Oh, B.S. Kim, I.J. Shon, Mechanical properties and rapid consolidation of nanostructured WC and WC-Al2O3 composites by high-frequency induction-heated sintering, Int. J. Refract. Metals Hard Mater. 58 (2016) 189–195, https://doi.org/10.1016/j.ijrmhm.2016.04.016.
[17] T. Csanádi, M. Bľanda, A. Duszová, N.Q. Chinh, P. Szommer, J. Dusza, Deformation characteristics of WC micropillars, J. Eur. Ceram. Soc. 34 (2014) 4099–4103, https://doi.org/10.1016/j.jeurceramsoc.2014.05.045.
[18] T. Dash, B.B. Nayak, Preparation of multi-phase composite of tungsten carbide, tungsten boride and carbon by arc plasma melting: characterization of melt-cast product, Ceram. Int. 42 (2016) 445–459, https://doi.org/10.1016/j.ceramint.2015.08.129.
[19] H. Jelitto, G.A. Schneider, Fracture toughness of porous materials e Experimental methods and data, Data Brief 23 (2019) 103709, https://doi.org/10.1016/j.dib.2019.103709.
[20] H. Jelitto, G.A. Schneider, A geometric model for the fracture toughness of porous materials, Acta Mater. 151 (2018) 443–453, https://doi.org/10.1016/j.actamat.2018.03.018.
[21] S.J. Bull, T.F. Page, E.H. Yoffe, An explanation of the indentation size effect in ceramics, Phil. Mag. Lett. 59 (1989) 281–288, https://doi.org/10.1080/09500838908206356.

[22] V.M. Sglavo, D.J. Green', INFLUENCE CONFIGURATION BEHAVIOUR OF OF INDENTATION CRACK ON STRENGTH AND FATIGUE SODA-LIME SILICATE GLASS, 1995.
[23] V.M. Sglavo, P. Pancheri, Crack Decorating Technique for Fracture-Toughness Measurement in Alumina, 1997.
[24] C. Relias, D. Ngai, Indentation Fracture Toughness: A Review and Application, vol. 97, American Ceramic Society Bulletin, 2018.
[25] D.K. Shetty, I.G. Wright, P.N. Mincer, A.H. Clauer, Indentation fracture of WC-Co cermets, J. Mater. Sci. 20 (1985) 1873–1882, https://doi.org/10.1007/BF00555296.
[26] G.R. Anstis, P. Chantikul, B.R. Lawn, D.B. Marshall, A critical evaluation of indentation techniques for measuring fracture toughness: I, direct crack measurements, J. Am. Ceram. Soc. 64 (1981) 533–538, https://doi.org/10.1111/j.1151-2916.1981.tb10320.x.
[27] L. Girardini, M. Zadra, F. Casari, A. Molinari, SPS, binderless WC powders, and the problem of sub carbide, Met. Powder Rep. 63 (2008) 18–22, https://doi.org/10.1016/S0026-0657(09)70039-6.
[28] L. Silvestroni, N. Gilli, A. Migliori, D. Sciti, J. Watts, G.E. Hilmas, W. G. Fahrenholtz, Binderless WC with high strength and toughness up to 1500 °C, J. Eur. Ceram. Soc. 40 (2020) 2287–2294, https://doi.org/10.1016/j.jeurceramsoc.2020.01.055.
[29] J. Poetschke, V. Richter, R. Holke, Influence and effectivity of VC and Cr 3C 2 grain growth inhibitors on sintering of binderless tungsten carbide, Int. J. Refract. Metals Hard Mater. 31 (2012) 218–223, https://doi.org/10.1016/j.ijrmhm.2011.11.006.
[30] L. Ortiz-Membrado, N. Cuadrado, D. Casellas, J.J. Roa, L. Llanes, E. Jiménez-Piqué, Measuring the fracture toughness of single WC grains of cemented carbides by means of microcantilever bending and micropillar splitting, Int. J. Refract. Metals Hard Mater. 98 (2021), https://doi.org/10.1016/j.ijrmhm.2021.105529.
[31] H. Taimatsu, S. Sugiyama, Y. Kodaira, Synthesis of W2C by reactive hot pressing and its mechanical properties, Mater. Trans. 49 (2008) 1256–1261, https://doi.org/10.2320/matertrans.MRA2007304.
[32] G.D. Quinn, R.C. Bradt, On the Vickers indentation fracture toughness test, J. Am. Ceram. Soc. 90 (2007) 673–680, https://doi.org/10.1111/j.1551-2916.2006.01482.x.
[33] W.D. Nix, H. Gao, Indentation size effects in crystalline materials: a law for strain gradient plasticity, J. Mech. Phys. Solid. 46 (1998) 411–425, https://doi.org/10.1016/S0022-5096(97)00086-0.
[34] K. Durst, B. Backes, O. Franke, M. Göken, Indentation size effect in metallic materials: modeling strength from pop-in to macroscopic hardness using geometrically necessary dislocations, Acta Mater. 54 (2006) 2547–2555, https://doi.org/10.1016/j.actamat.2006.01.036.
[35] A. Nino, A. Tanaka, S. Sugiyama, H. Taimatsu, Indentation size effect for the hardness of refractory carbides, Mater. Trans. 51 (2010) 1621–1626, https://doi.org/10.2320/matertrans.M2010110.
[36] K. Sangwal, Review: indentation size effect, indentation cracks and microhardness measurement of brittle crystalline solids - some basic concepts and trends, Cryst. Res. Technol. 44 (2009) 1019–1037, https://doi.org/10.1002/crat.200900385.
[37] B.J. Wachtman, W.R. Cannon, M.J. Matthewson, MECHANICAL PROPERTIES OF CERAMICS, 2009, https://doi.org/10.1002/9780470451519.